

Simulating the fire-thermal-structural behavior in a localized fire test on a bare steel beam¹

Chao Zhang^{a,b,*}, Hong-Xia Yu^c, Lisa Choe^b, John Gross^b, Guo-Hua Li^d

^aCollege of Civil Engineering, Tongji University, Shanghai 200092, China

^bNational Institute of Standards and Technology, 100 Bureau Drive, Gaithersburg, MD 20899-8666, USA

^cArup International, Beijing, China

^dBeijing University of Civil Engineering and Architecture, School of Civil and Transportation Engineering, Beijing 100037, China

Abstract

The engineering design practice may include fire protection design of steel structures in large volumes. Prescriptive methods in fire codes are based on the concept of fire compartmentation and might be inapplicable to large volumes. As an alternative, fire engineering performance based methods are developed, which may need sophisticated numerical models to adequately simulate the responses of structures in the design fire scenarios. This paper discusses an integrated fire-structural simulation model for performance based design. Sub-models were clearly described. The fire-structure simulation model was successfully applied to model the fire-thermal-structural behaviors in two localized fire tests on a real-scale steel beam recently conducted at the National Fire Research Laboratory (NFRL) of the National Institute of Standards and Technology (NIST). The model might be used in performance based structural fire safety design.

Keywords: fire-thermal-structural simulation; localized fire test; bare steel beam; performance-based design; FDS-FEM; coupling method.

1. Introduction

A large amount of effort was devoted to research on structural fire engineering in the past few decades and most of this work has assumed a post-flashover fire, which affects the entire building, or a fire compartment of the building, because it is generally believed that a post-flashover fire poses the largest risk to structural safety. Although the fire protection scheme might be rationalized with a structural fire engineering approach under such circumstances, fire mitigation strategies are still required. When the structure is subjected to low fire risk, typically unlikely to go to flashover, with fire risk analysis and subsequent structural fire

¹Cite this paper as: Zhang C., et al. (2018). "Simulating the fire-thermal-structural behavior in a localized fire test on a bare steel beam", *Engineering Structures*, Vol. 163, pp. 61-70.

*Currently guest scientist at NIST. E-mail address: chao.zhang@nist.gov(C. Zhang)

engineering design, a large amount of fire protection costs may be saved. Typical project examples include suspension bridges subjected to a lorry fire, large atriums with limited fuel load, etc. Models are developed for specific occasions. For example, the Steel Construction Institute (SCI) report [1] and the Eurocode 1 [2] include a calculation method for members outside a building facade and subjected to window fire. However, these empirical models only apply to a pre-defined, simplified fire situation, while, in reality, the space geometry, the structural form, and the fire location may all vary. It is very important that advanced tools be developed to simulate the combustion behavior in various environments and to evaluate the consequence of the fire on adjacent structural members.

Fig. 1 shows an example of an airport terminal in Beijing, China. The giant roof covers an area of approximately 76,000 m² and creates a huge indoor open space for the terminal. The roof is supported mainly by eight C-shaped columns with a span of over 100 m between the columns. The roof adopted a special grid system, which gradually mixed with the columns seamlessly. Fig. 1b shows the overall structural geometry of the roof and a localized view of a C-shaped column. Because of its huge size, the column is unlikely to be completely engulfed by a big fire. In the worst condition with a fire source right adjacent to the column, a few steel members will be directly impinged by fire while the majority of steel members will be near the fire. To appropriately evaluate the response of the structure in fire and then to design the fire protection scheme, it is essential to evaluate the influence of a possible fire to the column (e.g. nonlinear temperature distribution of the steel members), and, therefore, to have sophisticated fire-structure simulation models.

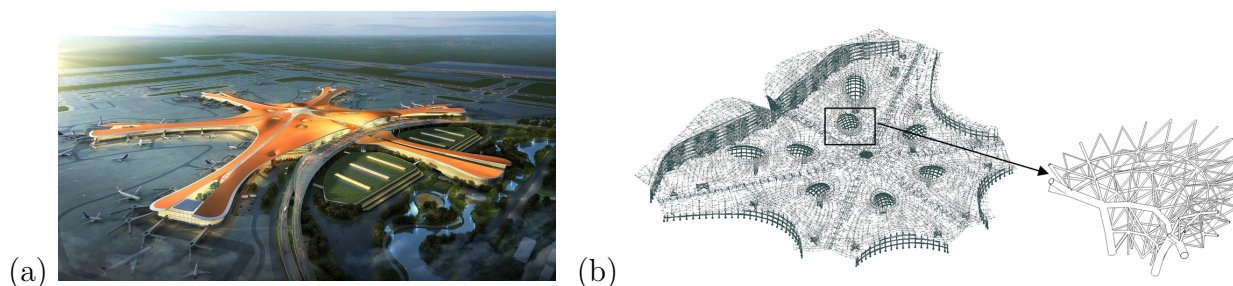


Figure 1: Beijing new airport terminal. (a) bird view; (b) structural form of the airport roof and a typical C-shaped column.

Fire-induced temperature rise has two effects on a structural component: it weakens mechanical properties and it causes thermal expansion. Restrained thermal expansion generates mechanical stress and the difference in thermal expansions causes thermal bowing [3]. Additionally, fire-induced asymmetrical temperature distribution may lead to a P - delta effect (or secondary moment) in compressive components [4]. The temperature degradation effect on structural materials has been well investigated and is considered in the current fire codes. Although many studies have shown that (restrained) thermal expansion can have a significant effect on load-bearing capacity of structural members, the effect of (restrained) thermal expansion is not considered in most fire codes. Experimental studies on the effects of fire-induced temperature gradients are limited. Available theoretical studies [4, 5, 6, 7]

show that ignoring fire-induced temperature gradient may be unconservative in evaluating the fire safety of steel structures in large enclosure (e.g. the steel column shown in Fig. 1).

2. Background

Most of the structural fire tests reported in literature are conducted in an enclosed furnace, some are conducted in real compartments (e.g. the Cardington full-scale fire tests [8]), and a small number are conducted in an open condition or a localized fire condition [9, 10, 11]. Furthermore, these tests seldom measure the heat release rate of the fire, which is the most important parameter in fire hazard assessment [12]. Recently, the National Institute of Standards and Technology added a unique facility named the National Fire Research Laboratory (NFRL), which allows for researchers to conduct tests on real-scale structural members and systems subjected to realistic fires [13]. This facility is equipped with an exhaust hood for fires up to 20 MW, a strong-floor, a strong-wall, and a structural loading apparatus to apply gravity loads on multi-story buildings. As part of commissioning the structural-fire test capabilities at the NFRL, a series of tests were conducted on loaded structural steel beams exposed to a localized fire [14]. Table 1 gives the matrix of the NFRL tests. In this paper, test 6, 7 and 8 were considered.

Table 1: Test matrix according to Ref. [14]

Test No.	BCs ^a	Fire load	Structural load
1,2	Simply supported	Natural gas fire (increased in 10 kW increments up to 500 kW)	Not applied
3,4,5	Simply supported	Natural gas fire (fixed at 400 kW)	Not applied
6	Simply supported	Not applied	Increased to failure
7	Simply supported	Fire1, steady-state heating	Force1
8	Simply supported	Fire2, transient heating	Force2
9	Shear connection	Fire2, transient heating	Force2

^aBoundary conditions at the end of the beam

In absence of test guidelines, an engineering approach was proposed by the authors to conduct pre-test simulations to design a testing fire for the NFRL experiments [15]. The approach adopts a simple analytical model to approximately calculate the critical value of heat release rate required to reach a target temperature in the test specimen and uses a sophisticated numerical model to verify/refine the calculation. The analytical model is developed by the first author in his previous work [16], which assumes the fire plume volume as a cylinder and uses the theory of heat radiation in participating medium to calculate the radiative heat fluxes to the horizontal surface (bottom surface of the beam specimen). The sophisticated numerical model is an integrated fire-structure model. As shown in Fig. 2,

the numerical model first uses the Fire Dynamics Simulator (FDS, introduced later in Section 3.1) [17] to simulate the realistic fire behavior and to predict the thermal boundary conditions of adiabatic surface temperatures (AST, introduced later in Section 3.2) and convective heat transfer coefficient (h_c) at the exposed surfaces of the structures considered; then, a fire-structure interface scheme or tool is used to transfer the data of thermal boundary conditions from the FDS model to a finite element (FE) thermal model and conduct a heat transfer analysis using the FE thermal model to get the temperature data (T_s) of the structures considered; and, finally, a load transfer method is used to map the steel temperature data (T_s) from the FE thermal model to a FE structural model and conduct a mechanical analysis to get the structural responses (deformations, stresses, strains, etc.). In [15], the proposed approach adequately predicted the critical value of heat release rate for the NFRL thermal tests (Tests 1 and 2 in Table 1), which demonstrates the capability of the approach for predicting the thermal boundary conditions in localized fires. In this paper, the sophisticated numerical model is used to simulate the NFRL structure fire tests (Tests 7 and 8 in Table 1), which intends to investigate the capacity of the model for predicting the temperature field and mechanical behavior of structures in realistic fires.

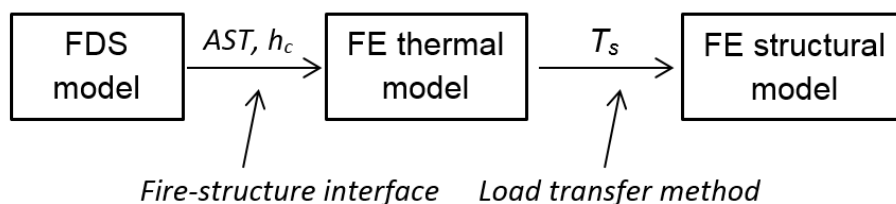


Figure 2: Illustration of the FDS-FEM simulation methodology.

3. Methodology

3.1. The FDS code

Fire Dynamics Simulator (FDS) is a large-eddy simulation (LES) based CFD (computational fluid dynamics) code [17]. For the simulations performed in this study, FDS version 6.2.0 was used. LES is a technique used to model the dissipative processes (viscosity, thermal conductivity, material diffusivity) that occur at length scales smaller than those that are explicitly resolved on the numerical grid. In FDS, the combustion is based on the mixing-limited, infinitely fast reaction of lumped species, which are reacting scalars that represent mixtures of species. Thermal radiation is computed by solving the radiation transport equation for gray gas using the Finite Volume Method (FVM) on the same grid as the flow solver. FVM is based on a discretization of the integral forms of the conservation equations. It divides the problem domain into a set of discrete control volumes (CVs) and node points are used within these CVs for interpolating appropriate field variables. The governing equations are approximated on one or more rectilinear grids. Obstructions with complex geometries

are approximated with groups of prescribed rectangles in FDS. One-dimensional (1D) heat conduction is assumed for solid-phase calculations. Note that a three dimensional heat conduction feature has been implemented in FDS and is in beta testing. Detailed descriptions of the mathematical models used in FDS can be found in [18].

3.2. Adiabatic surface temperature

Consider an ideal adiabatic surface exposed to a heating condition; the net heat flux to the surface is by definition zero, thus

$$\varepsilon_{AS}(\dot{q}_{in}'' - \sigma T_{AS}^4) + h_{c,AS}(T_g - T_{AS}) = 0 \quad (1)$$

where ε_{AS} is emissivity of the adiabatic surface; T_{AS} is temperature of the adiabatic surface or adiabatic surface temperature; T_g is temperature of the surrounding gas; $h_{c,AS}$ is convective heat transfer coefficient between the adiabatic surface and the surrounding gas; and σ is Stefan-Boltzmann constant, taken as $5.67 \times 10^{-8} \text{ W}/(\text{m}^2\text{K}^4)$.

From Eq. 1, the incident radiative flux to a surface can be calculated from an adiabatic surface temperature,

$$\dot{q}_{in}'' = \frac{h_{c,AS}(T_{AS} - T_g)}{\varepsilon_{AS}} + \sigma T_{AS}^4 \quad (2)$$

Accordingly, the net heat flux to a real surface with the same emissivity ($\varepsilon_{AS} = \varepsilon_s$), the same convective heat transfer coefficient ($h_{c,AS} = h_c$), and exposed to the same heating condition can be calculated by

$$\dot{q}_{net}'' = \varepsilon_s \sigma (T_{AS}^4 - T_s^4) + h_c (T_{AS} - T_s) \quad (3)$$

where T_s is temperature of the real surface. Eq. 3 shows that the net heat flux to a surface can be approximately calculated by using a single parameter T_{AS} . In practice, the adiabatic surface temperatures of interest can be approximately measured by a plate thermometer. FDS [17] includes an output quantity of adiabatic surface temperature calculated by Eq. 3 according to the method proposed by Wickstrom [19]. It should be noted that the calculated adiabatic temperature of a surface is fundamentally influenced by the convective heat transfer coefficient and surface emissivity [20, 21].

3.3. Fire-structure interface

The DEVICE approach described in [22] was used to transfer data from FDS model to FE thermal model. By that approach, point measurements (devices) are used in FDS to record the adiabatic surface temperatures. The output adiabatic surface temperatures and convective heat transfer coefficients are converted to inputs to the FE thermal model. The data points are interpreted as the effective black body temperature and bulk (gas) temperature to calculate the radiative and convective heat fluxes to the structural elements, respectively. The adiabatic surface temperature between the two measurement points are determined by linear interpolation.

3.4. Elevated temperature material model

Thermal properties for structural steel specified in the Eurocode 3 [23] were used. The thermal expansion coefficient for structural steel recommended by NIST TN 1681 [24] was used:

$$\alpha_s = 1.17 \times 10^{-5} + 1.34 \times 10^{-8}T - 9.7 \times 10^{-12}T^2 + 1.67 \times 10^{-16}T^3 \quad (4)$$

where α_s is thermal expansion coefficient of steel; and T is temperature of steel.

The stress-strain model for structural steel developed by Luecke et al. [25] was used:

$$\sigma = \epsilon E_T \quad \left(\epsilon \leq \frac{f_{yT}}{E_T}\right) \quad (5a)$$

$$\sigma = f_{yT} + (k_3 - k_4 f_{y20}) \exp\left[-\left(\frac{T}{k_2}\right)^{k_1}\right] \left(\epsilon - \frac{f_{yT}}{E_T}\right)^n \quad \left(\epsilon \geq \frac{f_{yT}}{E_T}\right) \quad (5b)$$

with $k_1 = 7.820$, $k_2 = 540$ °C, $k_3 = 1006$ MPa, $k_4 = 0.759$, and $n = 0.503$. Here, σ and ϵ are stress and strain. The elastic modulus and yield strength at elevated temperature are given by

$$\frac{E_T}{E_{20}} = \exp\left[-\frac{1}{2}\left(\frac{T-20}{639}\right)^{3.768} - \frac{1}{2}\left(\frac{T-20}{1650}\right)\right] \quad (6)$$

and

$$\frac{f_{yT}}{f_{y20}} = 0.09 + 0.91 \exp\left[-\frac{1}{2}\left(\frac{T-20}{588}\right)^{7.514} - \frac{1}{2}\left(\frac{T-20}{676}\right)\right] \quad (7)$$

respectively. E_{20} , E_T are elastic modulus of steel at room and elevated temperatures; and f_{y20} , f_{yT} are yield strength of steel at room and elevated temperatures. This constitutive model was selected for its better representation of the high temperature tensile coupon test data [26].

4. Experimental description

Fig. 3a shows a schematic of the test setup, which was composed of the W16x26 beam specimen, reaction frames, and HSS (hollow structural section) loading beams. No fire protection was applied to the test specimen. All the components of structural steel frames were designed in accordance with the ANSI/AISC-360 (2010). Fig. 3b shows the dimensions of the beam specimen and the loading beams. The length of the beam specimen was (6.17 ± 0.02) m. The beam specimen was simply supported with the bearing-to-bearing length of (5.86 ± 0.02) m. The distance from the centroid of the beam cross section to the strong floor was (1.8 ± 0.01) m. Two HSS loading beams were placed at (2.44 ± 0.01) m apart. The ends of the beam specimen and the regions in contact with the HSS loading beams were laterally restrained. The lengths of the HSS loading beams were (6.71 ± 0.02) m. The HSS loading beams were pulled down via high strength rods at their ends which were connected to four actuators mounted underside of the strong floor. Hence, a uniform bending moment was applied in the beam specimen between the location of two loading beams throughout the tests. The fuel delivery system consisted of two natural gas burners with a nominal flame zone of one square meter to provide heat release rate (HRR) up to 1.5 MW, as shown

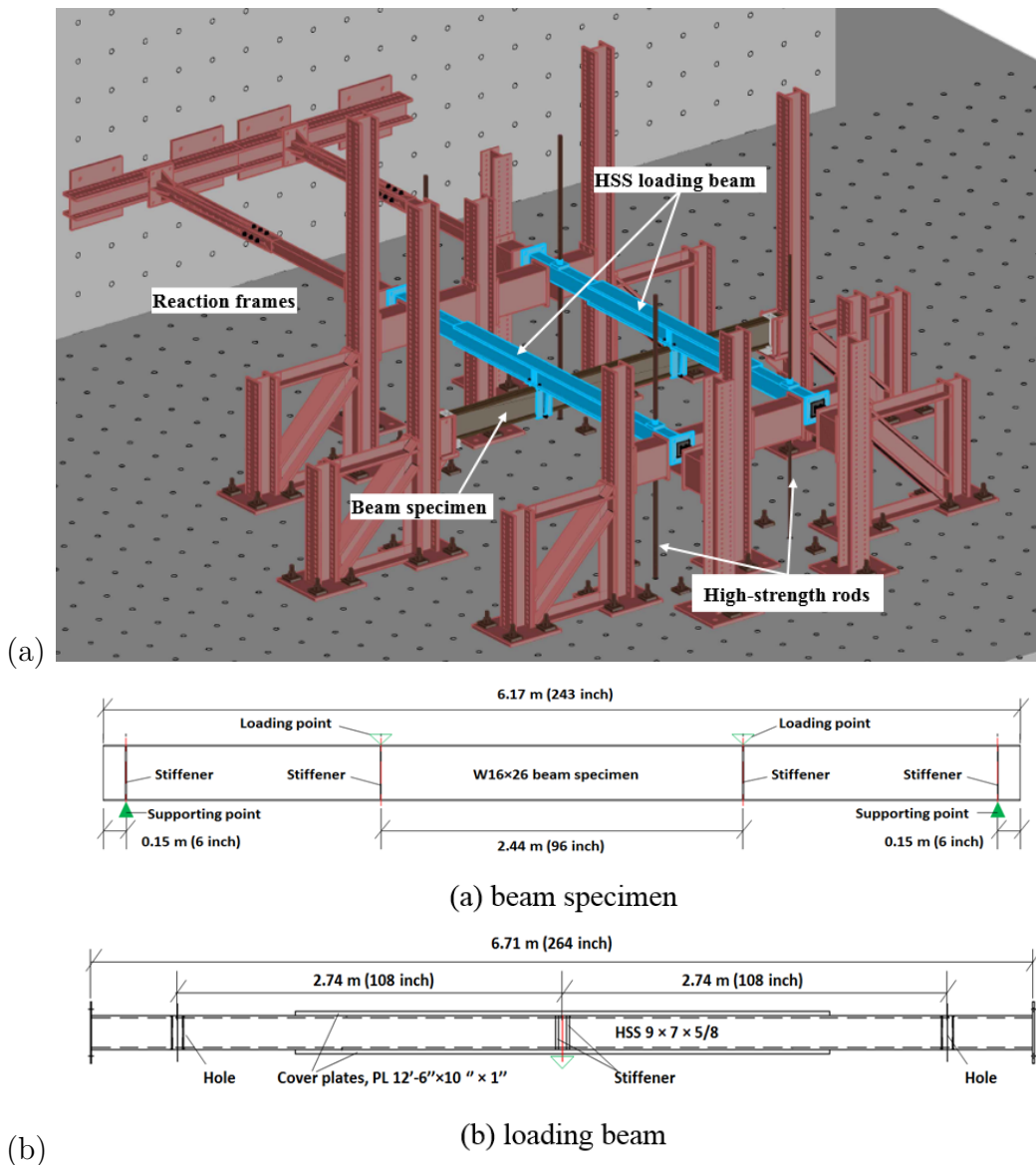


Figure 3: Experimental design [14]. (a) test setup; (b) Dimensions of the beam specimen and the loading beam.

in Fig. 4. The distance from the bottom side of lower flange of the beam specimen to the top surface of the burners was (1.1 ± 0.1) m.

The steady test (Test 7 in Table 1) was conducted in two steps as follows: i) The *HRR* of the burner was fixed at a target magnitude of 700 kW. ii) After the temperature at the fire-exposed bottom flange of the steel beam reached the steady-state condition, two point loads increased at a rate of 2 kip/min (8.90 kN/min) simultaneously until the failure occurred (Fig. 5a). In the transient test (Test 8 in Table 1), the beam specimen was loaded to 67% of the room temperature capacity at ambient temperature, which was similar to the critical load obtained from the steady test. While the load was maintained, the natural gas

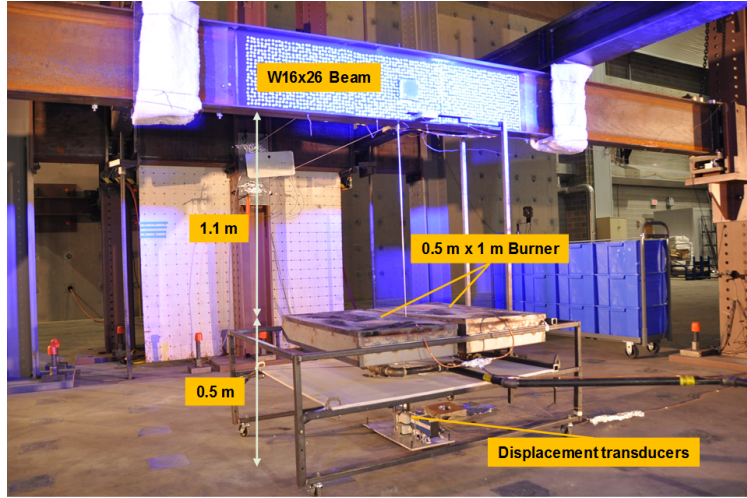


Figure 4: Photograph of burner in the test setup. The specimen looks blue because blue light was applied in the test so that digital image camera could see through the flame.

burner increased heat release rates following an arbitrary t-squared function ($[4.5t^2 + 250]$ kW \leq 1600 kW, t in min) to apply transient heating conditions to the specimen until failure occurred (Fig. 5b).

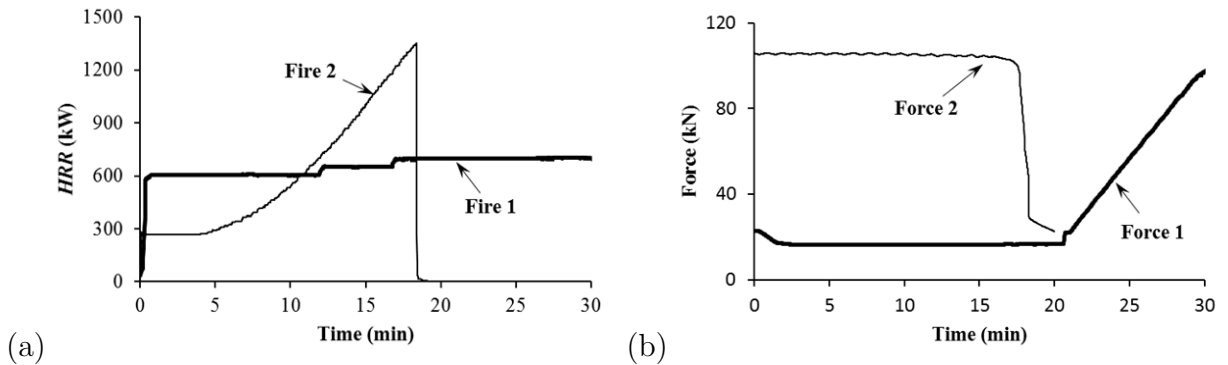


Figure 5: Fire loads and structural loads. (a) heat release rate curves; (b) applied forces.

In the steady and transient tests, zero was derived from instrument specifications, while the thermocouple installation error was estimated from past experience. The test repeatability and random was estimated by statistical means. The components of combined uncertainty for temperature included manufacturers specifications on zero error of $\pm 1\%$, installation error of $\pm 2\%$, random error of $\pm 2\%$, and test repeatability of $\pm 5\%$. The measured temperatures have a total expanded uncertainty of $\pm 12\%$ which was calculated from a combined uncertainty of $\pm 6\%$ and a coverage factor of 2 with a level of confidence of approximately 95 percent. The uncertainty in the HRR measurements with a natural gas burner is presented in Ref. [14] and not presented here for brevity.

5. Fire modeling

5.1. The FDS model

Fig. 6 shows the FDS model geometry and computational meshes for the NFRL structural fire tests. The green dots are the devices used to measure the thermal boundary conditions (adiabatic surface temperatures and film coefficients). Dimensions of the computational domain were 7.2 m (X) \times 1.2 m (Y) \times 3.6 m (Z). The grid size used is an important numerical parameter in CFD because of its impact on numerical accuracy. Three meshes were considered in this study. For mesh 1, uniform grids of 4 cm were used in the Y and Z directions, and mid-stretched grid was used in the X direction (the smallest grid size was 4 cm); for mesh 2, uniform grids of 2 cm were used in the Y and Z directions, and mid-stretched grid was used in the X direction (the smallest grid size was 2 cm); and for mesh 3, mid-stretched grids were used in X, Y and Z directions (the smallest grid size was 2 cm). Therefore, the computational domain consisted of 291,600 control volumes for mesh 1, 1,555,200 control volumes for mesh 2, and 388,800 control volumes for mesh 3.

In the FDS numerical model, the steel sections were modeled by obstructions with zero thickness. The default solid boundary condition in FDS, named “INERT”, and a user-defined solid boundary condition, named “STEEL” were used. For the “INERT” boundary condition, the temperature of the solid was taken as the ambient temperature during the simulation; and for the “STEEL” boundary condition, the temperature of the solid is changing and is calculated using the thermal properties of structural steel specified in Section 3.4. In engineering design practice, the thermal properties of building materials are usually unknown and the “INERT” boundary condition is usually assumed. Note that because of the 1D heat conduction assumption, the solid temperatures predicted by FDS can be significantly different from the temperatures calculated using 3D heat conduction model. Therefore, using other solid boundary conditions in FDS cannot be justified to be a better choice when 3D heat conduction is important.

5.2. FDS results

Generally, a finer mesh gives more accurate numerical results, and, at the same time, requires more physical running time. For a computational time of 1843 seconds, the running for the mesh 1 FDS model uses 18 CPU cores in the FDS simulation cluster maintained by NIST and takes 1 day 11 hours and 21 minutes (physical time); for the mesh 2 FDS model uses 24 CPU cores and takes 11 days 14 hours and 30 minutes; and for the mesh 3 FDS model uses 12 CPU cores and takes 5 days 1 hour and 8 minutes.

Fig. 7 shows the FDS simulated flame geometry for various *HRR*s. Note that flame shape changes with time because of the turbulent combustion processes. The video recorded flame behaviors were also presented. Fig. 8 shows the FDS predicted adiabatic surface temperatures for the mid-section of the beam specimen. The adiabatic surface temperature at the bottom surface (Point 1) increases with *HRR* until a steady value because the portion of the flame that contributes radiation to the bottom surface becomes constant once *HRR* reaches a critical value. With *HRR* increases, the adiabatic surface temperature of the top surface of the upper flange (Point 7) is first lower and then higher than that of the bottom

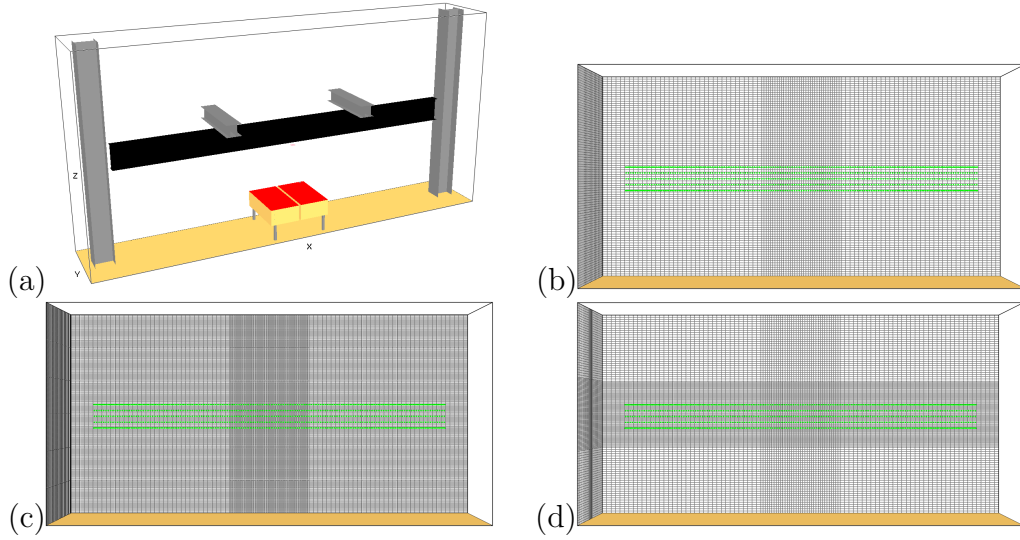


Figure 6: FDS numerical model. (a) geometry; (b) mesh 1; (c) mesh 2; (d) mesh 3.

surface of the upper flange (Point 5), which is also because of the change of flame behavior as shown in Fig. 7.

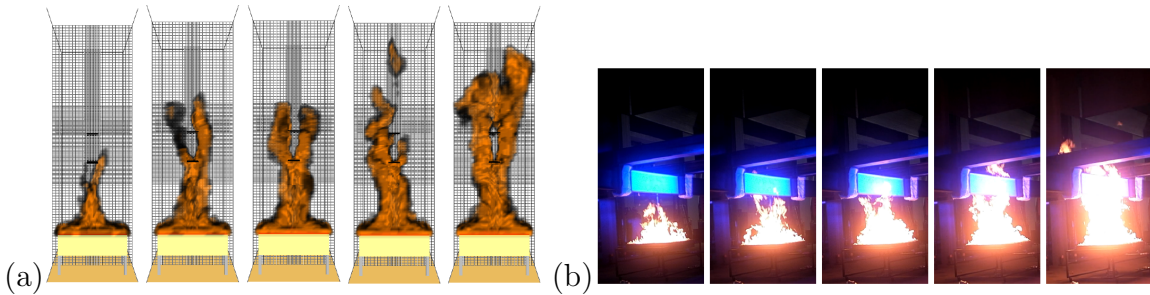


Figure 7: Simulated (a) and measured (b) flame behaviors for various HRR s (300 kW to 1100 kW with increment HRR of 200 kW). The numerical results are from the FDS model with mesh 3 and “INERT” solid boundary condition. The specimen looks blue because blue light was applied in the test so that digital image camera could see through the flame.

For the bottom surface of the beam specimen, meshes 1, 2 and 3 gave consistent prediction of adiabatic surface temperature; and for other surfaces, meshes 2 and 3 gave consistent prediction while mesh 1 gave higher prediction. The higher prediction of mesh 1 might be explained by the difference in the predicted flame behavior as shown in Fig. 9. Mesh 1 model failed to capture the turbulence behavior around the beam section.

For the bottom and top surfaces of the beam specimen, the “INERT” and “STEEL” solid boundary conditions gave consistent prediction of the adiabatic surface temperature; and for other surfaces, the “STEEL” solid boundary condition gave higher prediction. This could be explained by the fact that for the bottom and top surfaces of the beam specimen, the incident radiative heat fluxes are solely from the flame, while for the other surfaces, the incident radiative heat fluxes also include irradiation from the surrounding steel surfaces.

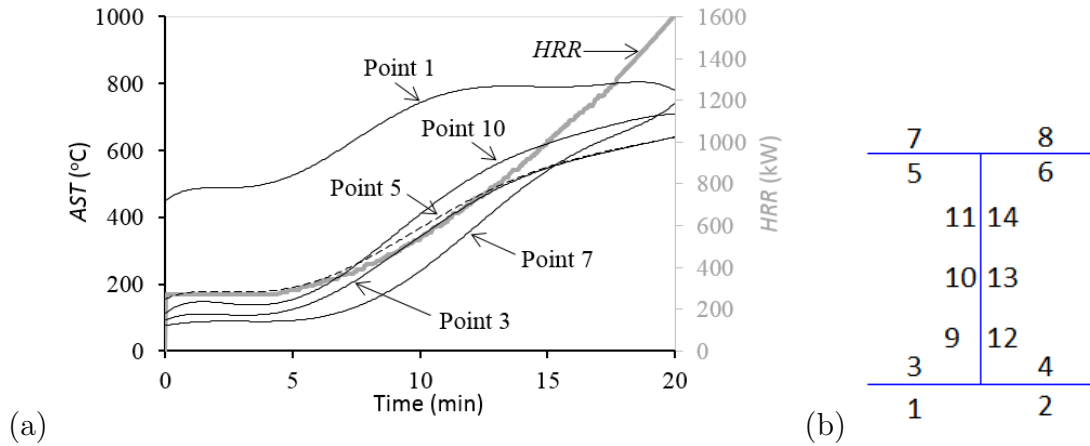


Figure 8: Predicted adiabatic surface temperatures for the mid-section of the beam specimen. (a) results; (b) location of points. The numerical results are from the FDS model with mesh 3 and “INERT” solid boundary condition.

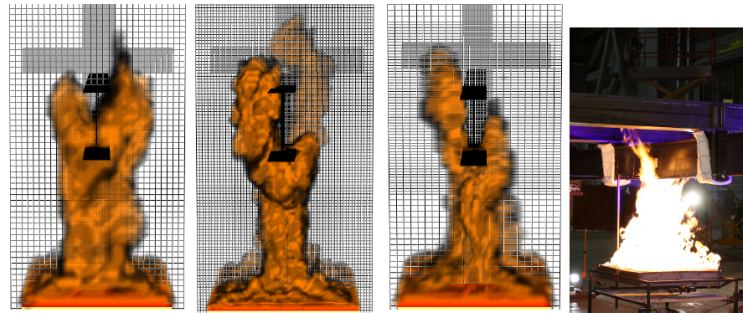


Figure 9: FDS predicted flame geometry (for the steady test) at 925.2 s after ignition for different meshes. A test photograph is also included for comparison. Left to right are numerical results with mesh 1 to 3.

6. Thermal-structural modeling

6.1. The FE models

Fig. 10a shows the FE structural model for the NFRL test setup with simply supported boundary conditions (Test 6, 7 and 8). The beam specimen and the loading beams were meshed with the structural shell element SHELL181 in ANSYS² [27]. The divisions of the beam specimen were 8 for flanges, 12 for web and 210 along beam length, and the divisions of the tubes of the loading beams were 4 for flanges, 6 for web and 180 along beam length. The axial displacements (along Z direction in the FE model) of the loading beams were restrained (see ① in Fig. 10). The lateral displacements (along X direction) of the loading beams were restrained at the loading points (see ②). To model the simply

²Certain commercial entities, equipment, or materials may be identified in this document in order to describe an experimental procedure or concept adequately. Such identification is not intended to imply recommendation or endorsement by the National Institute of Standards and Technology, nor is it intended to imply that the entities, materials, or equipment are necessarily the best available for the purpose.

supported boundary conditions, the vertical displacements (along Z direction) of the nodes of the lower flange at the support and the lateral displacements (along X direction) of the four corner nodes were restrained (see ③ or ④). At the intersection of the beam specimen and the loading beam, the lateral displacements of the exterior nodes of the stiffener, the four corner nodes of the beam specimen, and the nodes at the bottom of the loading beam were coupled (⑤). At the intersection, the vertical displacements (along Y direction) of the nodes of the upper flange of the beam specimen and the nodes of the bottom of the loading beam were also coupled (⑤). Concentration forces or displacements were applied along the lines on the top of the loading beams (see ②). Initial geometrical imperfection in the test specimen was measured and the measured amplitude of $L/900$ was applied in the FE model. Here, L is the length of beam specimen. The measured shape of initial geometrical imperfection was not used, instead the shape was defined as the first mode obtained from elastic buckling analysis of an isolated beam specimen under compression. Residual stress was not considered in the FE model.

The FE thermal model only included the beam specimen which was meshed with the thermal shell element SHELL131 in ANSYS. The divisions of the beam specimen were the same as for the FE structural model. The adiabatic surface temperatures predicted by FDS were applied to the external nodes, and the film coefficients predicted by FDS were applied to the exposed surfaces, as shown in Fig. 10b. The tubes of the loading beams were filled with flowing water during the fire test and the temperatures of the loading beams were assumed to be ambient temperature during the fire test. The heat transfer at the intersections between the beam specimen and the loading beams were ignored.

The steel for the beam specimen is ASTM A992, for the HSS section is ASTM A500 Gr. B and for the cover plate of the loading beam is ASTM A36. The ambient temperature yield strength for the steel of the beam specimen was measured by the steel fabricator and the measured value of 440 ± 1.15 MPa was used in the FE structural model. Here, the standard uncertainty is estimated based on the certified material test report provided by steel fabricator and assumption of uniform distribution. The numbers following the symbol \pm are the expanded uncertainty with a level of confidence of approximately 95%. The ambient temperature yield strength for steels of the HSS section (ASTM A500 Gr.B) and cover plate (ASTM A36) were not measured, and the nominal yield strengths were used in the FE structural model. The high temperature mechanical properties were not measured and the constitutive model developed by Luecke et al. [25] was selected for its better representation of the tensile coupon test data [26]. The thermal expansion coefficient for structural steel recommended by NIST TN 1681 [24] was used. The thermal properties for structural steel given in the Eurocode 3 [23] were used.

6.2. FE results for ambient test

Before fire tests, ambient test (Test 6 in Table 1) on the beam specimen was conducted to study the failure behavior and ultimate load. Displacement control method was used to apply load. To investigate the capacity of the developed FE structural model, the ambient test was simulated. Fig. 11 shows the predicted load-displacement curves for the ambient test. The test data are also presented. The beam specimen failed by lateral torsional

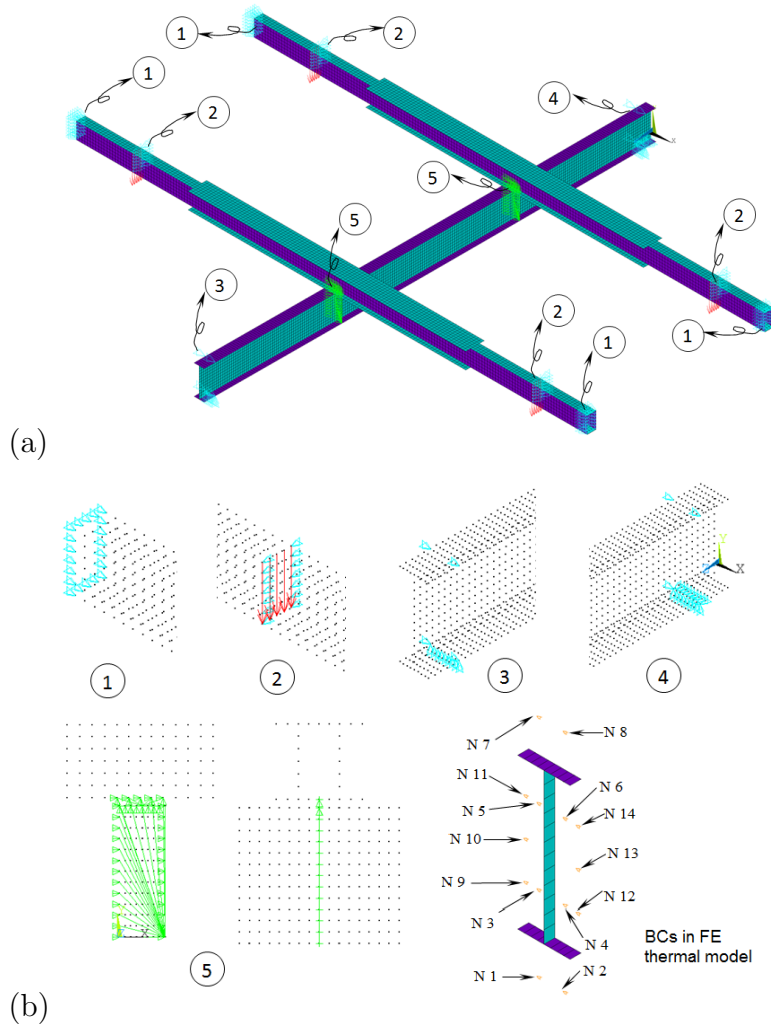


Figure 10: Finite element models. (a) FE structural model; (b) boundary conditions in FE models.

buckling and the measured maximum reaction force is 146 kN. In FE simulation, a linearly increasing displacement was simultaneously applied at the four load cells (② in Fig. 10) and the predicted maximum reaction force is 152 kN. The divergences between the predicted and measured curves might be caused by the uncertainty of the material model and the friction effects (between loading beam and test specimen) during the test.

6.3. FE results for steel temperature

Fig. 12a shows the non-uniform temperature distribution in the beam specimen. Fig. 13 shows the FEM predicted steel temperatures at the mid-section of the beam specimen. The measured temperatures were also plotted for comparison. In the tests, thermocouples were symmetrically installed to measure the temperatures of the bottom and top flanges (Fig. 12b). Average values of the thermocouples located at symmetric positions were plotted. The plotted web temperatures were the temperatures at the mid of the web (Fig. 12b).

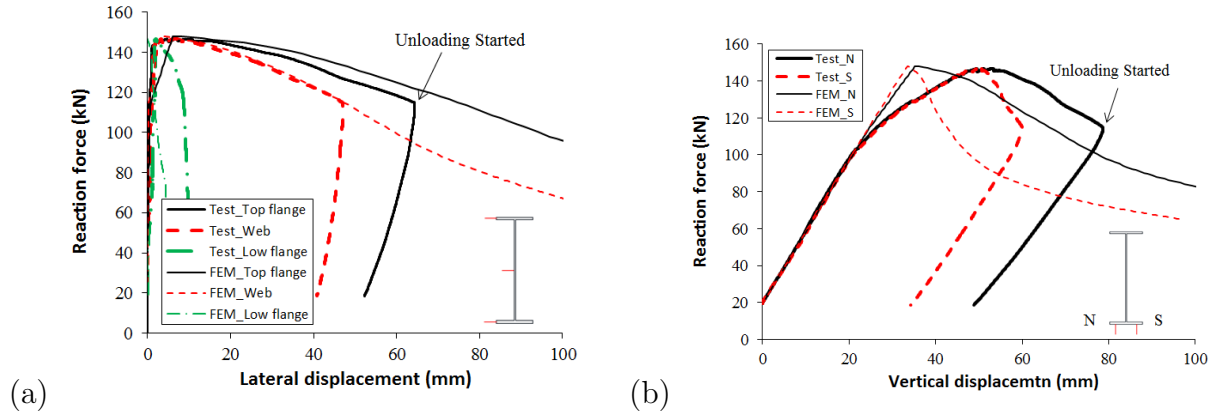


Figure 11: FE predictions against test data for the NFRL ambient beat test. (a) reaction force vs lateral displacement; (b) reaction force vs vertical displacement.

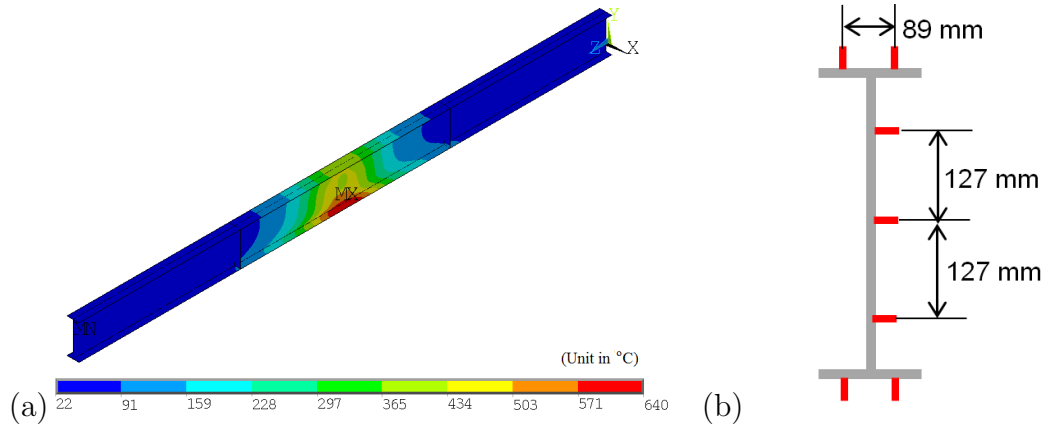


Figure 12: Predicted steel temperature distribution at 1840 s in Fire1 (Test 7). (a) results; (b) location of thermal couples.

For the steady test, the predicted bottom flange and the mid-web temperatures agreed well with the test data, while the predicted top flange temperature was slightly higher. The over-prediction of the top-flange temperature could be mainly caused by the over-prediction of the adiabatic surface temperature as found for the simulation of the NFRL thermal test (Test 3 in Table 1) in Ref. [15]. The differences among the predicted and measured maximum temperatures for bottom flange, mid-web, and top flange were $635\text{ }^{\circ}\text{C} - 654\text{ }^{\circ}\text{C} = -19\text{ }^{\circ}\text{C}$ (-2.9 %), $397\text{ }^{\circ}\text{C} - 437\text{ }^{\circ}\text{C} = -40\text{ }^{\circ}\text{C}$ (-9.4 %), and $411\text{ }^{\circ}\text{C} - 350\text{ }^{\circ}\text{C} = 61\text{ }^{\circ}\text{C}$ (17.4 %), respectively. For the transient test, the predicted bottom flange temperatures agreed well with the test data, while the predicted mid-web and top flange temperatures considerably diverged from the test data at temperatures above 200 °C. Those divergences of the measured and predicted steel temperatures could be mainly caused by the differences in the measured and predicted adiabatic surface temperatures, as found in Ref. [15]. When fire extinguished in the transient test, the differences among the predicted and measured temperatures for bottom flange, mid-web and top flange were $671\text{ }^{\circ}\text{C} - 705\text{ }^{\circ}\text{C} = 34\text{ }^{\circ}\text{C}$ (-5.0

%), $638\text{ }^{\circ}\text{C} - 534\text{ }^{\circ}\text{C} = 104\text{ }^{\circ}\text{C}$ (19.5 %) and $540\text{ }^{\circ}\text{C} - 410\text{ }^{\circ}\text{C} = 130\text{ }^{\circ}\text{C}$ (31.7%), respectively.

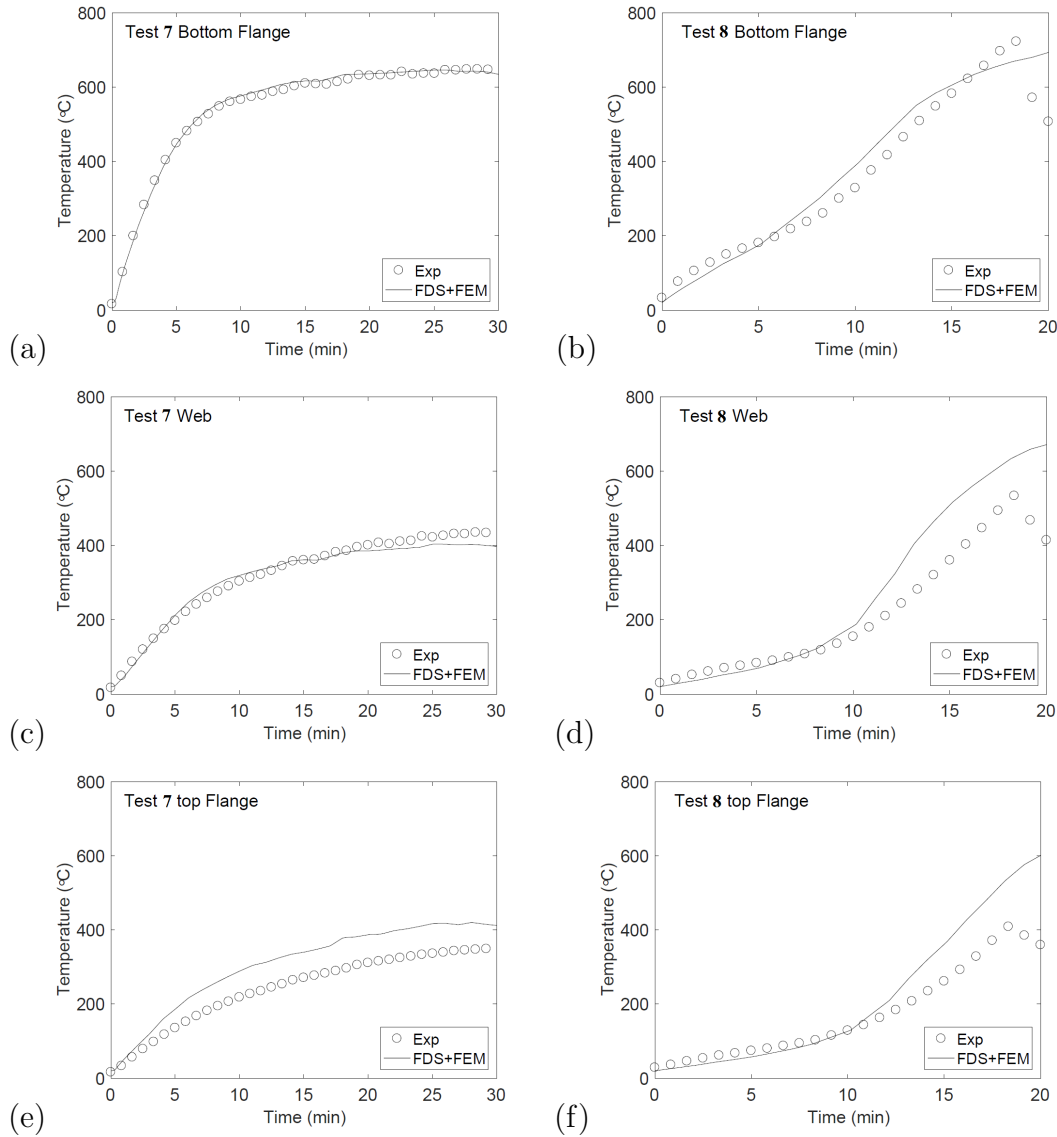


Figure 13: Comparison between the predicted and measured steel temperatures in the center section of the beam specimen exposed to the steady (left) and the transient (right) fires. (a)-(b) bottom flange temperatures; (c)-(d) web temperatures; (e)-(f) top flange temperatures

6.4. FE results for structural response

Fig. 14 compares the predicted and observed failure behavior of the beam specimen in the steady fire test. Fig. 15 compares the measured and predicted vertical displacements for the steady and transient tests. For the steady test, the vertical displacement measured at the bottom of the mid-section of the beam specimen was used. For the transient tests, the average vertical displacements measured at the bottom of the intersections between the

beam specimen and the loading beam were used because the potentiometers used to measure the vertical displacement at the mid-section were broken during test. The beam specimen failed by lateral torsional buckling in all the steady and transient tests. For the steady test, the differences among predicted and measured failure time, failure temperature and failure load were $30.8 \text{ min} - 30.6 \text{ min} = 0.2 \text{ min}$ (0.7%), $635 \text{ }^\circ\text{C} - 654 \text{ }^\circ\text{C} = -19 \text{ }^\circ\text{C}$ (-2.9%) and $102 \text{ kN} - 100 \text{ kN} = 2 \text{ kN}$ (2%), respectively. For the transient test, the difference between the predicted and measured failure time and failure temperature were $16.5 \text{ min} - 17.7 \text{ min} = -1.2 \text{ min}$ (-6.8%) and $640 \text{ }^\circ\text{C} - 706 \text{ }^\circ\text{C} = -66 \text{ }^\circ\text{C}$ (9.3%), respectively.

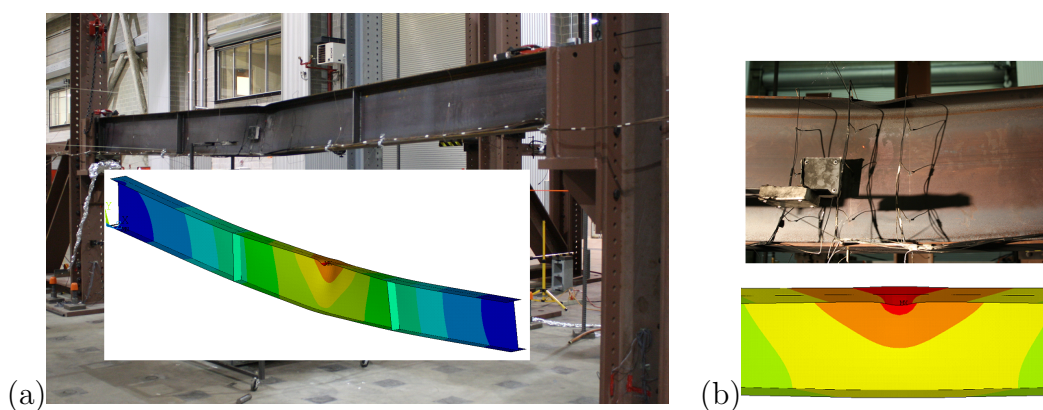


Figure 14: Predicted and measured structural failure mode for the steady test (Test 7). (a) global deformation; (b) local deformation.

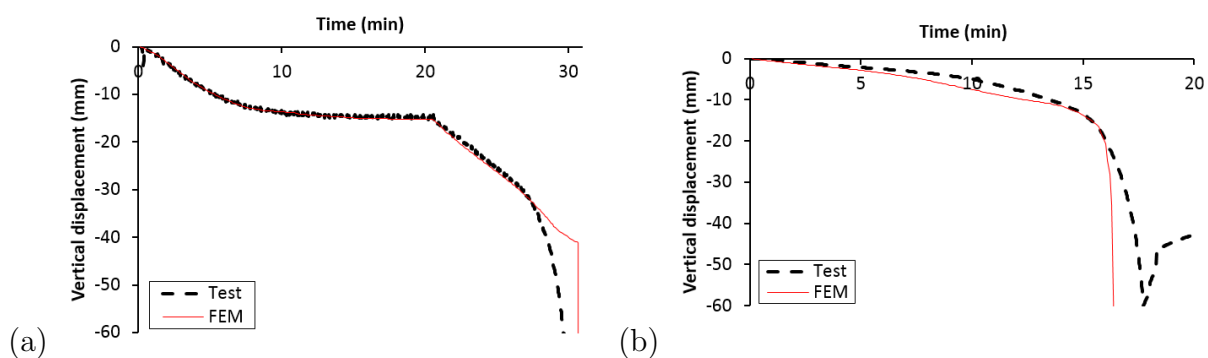


Figure 15: Predicted and measured vertical displacements of the beam specimen. (a) steady test (Test 7); (b) transient test (Test 8).

7. CONCLUSIONS

Engineering structures may have complex geometry and in some situations are subjected to low fire risk, typically unlikely to go to flashover. In those cases, with fire risk analysis and subsequent structural fire engineering design, a large amount of fire protection may be saved. Sophisticated numerical models, capable of adequately predict the performance of

structures under realistic scenarios, may be required in a structural fire engineering design. This paper fills the gap between engineering demand for sophisticated numerical tools and laboratory research to collect technical data. The successful prediction of the failure temperature (within error of 10%) and failure time (within error of 7%) in two localized fire tests on a loaded bare steel beam provide validation points for structural fire engineers to gain confidence in using FDS with coupled numerical tools (e.g., finite-element models) in performance-based fire safety design.

Acknowledgements

Thanks to Drs. Randall McDermott and Kevin McGrattan of NIST for their support in developing and improving the numerical models. Thanks to Dr. Selvarajah Ramesh for his help in providing the uncertainties of the test data. Valuable suggestions and review comments from Dr. Kevin McGrattan, Dr. Joseph Main, Dr. Matthew Bundy and Mr. Nelson Bryner of NIST are acknowledged. CZ acknowledges support by the National Nature Science Foundation of China under Grant 51508399.

References

- [1] L. Margaret, O. Turlogh, Fire and steel constructions - fire safety of bare external structural steel, Steel Construction Institute, 1990.
- [2] BSI, Eurocode 1: Actions on structures - Part 1-2: General rules - Actions on structures exposed to fire, British Standard, 2002.
- [3] A. Usmani, J. Rotter, S. Lamont, A. Sanad, M. Gillie, Fundamental principles of structural behaviour under thermal effects, *Fire Safety Journal* 36 (2001) 721–744. doi:10.1016/S0379-7112(01)00037-6.
- [4] C. Zhang, J. Gross, T. McAllister, G. Li., Behavior of unrestrained and restrained bare steel columns subjected to localized fire, *Journal of Structural Engineering-ASCE* 141. doi:10.1061/(ASCE)ST.1943-541X.0001225.
- [5] C. Zhang, G. Li, A. Usmani, Simulating the behavior of restrained steel beams to flame impinged localized fires, *Journal of Constructional Steel Research* 83 (2013) 156–65.
- [6] C. Zhang, J. Gross, T. McAllister, Lateral torsional buckling of steel w-beams to localized fires, *Journal of Constructional Steel Research* 88 (2013) 330–8. doi:10.1016/j.jcsr.2013.06.004.
- [7] A. Agarwal, L. Choe, A. Varma, Fire design of steel columns: effects of thermal gradients, *Journal of Constructional Steel Research* 93 (2014) 107–18. doi:10.1016/j.jcsr.2013.10.023.
- [8] B. Kirby, The behaviour of a multi-story steel framed building subjected to fire attack, experimental data, Tech. rep., British Steel (2000).
- [9] D. Kamikawa, Y. Hasemi, K. Yamada, M. Nakamura, Mechanical response of a steel column exposed to a localized fire, in: *Proceedings of the Fourth International Workshop on Structures in Fire*, Aveiro, Portugal, 2006, pp. 225–34.
- [10] A. Bystrom, J. Sjostrom, M. V. U. Wickstrom, Large scale test to explore thermal exposure of column exposed to localized fire, in: *Proceedings of the 7th International Conference on Structures in Fire*, 2012, pp. 185–194.
- [11] G. Ferraz, A. Santiago, J. Rodrigues, P. Barata, Thermal analysis of hollow steel columns exposed to localized fires, *Fire Technology* 52 (2016) 663–681. doi:10.1007/s10694-015-0481-2.
- [12] V. Babrauskas, R. Peacock, Heat release rate: The single most important variable in fire hazard, *Fire Safety Journal* 18 (1992) 255–272. doi:10.1016/0379-7112(92)90019-9.
- [13] M. Bundy, A. Hamins, J. Gross, W. Grosshandler, L. Choe, Structural fire experimental capabilities at the nist national fire research laboratory, *Fire Technology* 52 (2016) 959966. doi:10.1007/s10694-015-0544-4.

- [14] L. Choe, S. Ramesh, M. Hoehler, M. Seif, C. Zhang, J. Gross, M. Bundy, National Fire Research Laboratory Commissioning Project: Testing steel beams under localized fire exposure, NIST technical note 1977, National Institute of Standards and Technology (2017).
- [15] C. Zhang, L. Choe, J. Gross, S. Ramesh, M. Bundy, Engineering approach for designing a thermal test of real-scale steel beam exposed to localized fire, *Fire Technology* doi:10.1007/s10694-016-0646-7.
- [16] C. Zhang, A. Usmani, Heat transfer principles in thermal calculation of structures in fire, *Fire Safety Journal* 78 (2015) 85–95. doi:10.1016/j.firesaf.2015.08.006.
- [17] K. McGrattan, S. Hostikka, R. McDermott, J. Floyd, C. Weinschenk, K. Overholt, Fire Dynamics Simulator, User’s Guide, National Institute of Standards and Technology, Gaithersburg, Maryland, USA, and VTT Technical Research Centre of Finland, Espoo, Finland, sixth Edition (September 2013).
- [18] K. McGrattan, S. Hostikka, R. McDermott, J. Floyd, C. Weinschenk, K. Overholt, Fire Dynamics Simulator, Technical Reference Guide, National Institute of Standards and Technology, Gaithersburg, Maryland, USA, and VTT Technical Research Centre of Finland, Espoo, Finland, sixth Edition, vol. 1: Mathematical Model; Vol. 2: Verification Guide; Vol. 3: Validation Guide; Vol. 4: Configuration Management Plan (September 2013).
- [19] U. Wickstrom, D. Duthinh, K. McGrattan, Adiabatic surface temperature for calculating heat transfer to fire exposed structures, in: *Proceedings of the 11th International Interflam Conference*, London, England, 2007, pp. 943–53.
- [20] C. Zhang, G. Li, R. Wang, Using adiabatic surface temperature for thermal calculation of steel members exposed to localized fires, *International Journal of Steel Structures* 13 (2013) 547–58. doi:10.1007/s13296-013-3013-2.
- [21] A. Andreozzi, N. Bianco, M. Musto, G. Rotondo, Adiabatic surface temperature as thermal/structural parameter in fire modeling: thermal analysis for different wall conductivities, *Applied Thermal Engineering* 65 (2014) 422–432. doi:10.1016/j.applthermaleng.2014.01.036.
- [22] C. Zhang, J. Silva, C. Weinschenk, D. Kamikawa, Y. Hasemi, Simulation methodology for coupled fire-structure analysis: modeling localized fire tests on a steel column, *Fire Technology* 52 (2015) 239–262. doi:10.1007/s10694-015-0495-9.
- [23] BSI, Eurocode 3: Design of steel structures - Part 1-2: General rules - Structural fire design, British Standard, 2005.
- [24] L. Phan, T. McAllister, J. Gross, M. Hurley, Best practice guidelines for structural fire resistance design of concrete and steel buildings, NIST technical note 1681, National Institute of Standards and Technology (NIST), Gaithersburg, Maryland (2010). doi:10.6028/NIST.TN.1681.
- [25] W. E. Luecke, S. Banovic, J. McColskey, High-temperature tensile constitutive data and models for structural steels in fire, NIST technical note 1714, National Institute of Standards and Technology (NIST), Gaithersburg, Maryland (2011). doi:10.6028/NIST.TN.1714.
- [26] L. Choe, C. Zhang, W. Luecke, J. Gross, A. Varma, Influence of material models on predicting the fire behavior of steel columns, *Fire Technology* doi:10.1007/s10694-016-0568-4.
- [27] ANSYS, ANSYS User Manual, Version 14.0, ANSYS Inc., 2012.